1-2024

Toward the Unified Theory of SAID-Linked Subauroral Arcs

Evgeny V. Mishin
Air Force Research Laboratory, evgeny.mishin@spaceforce.mil

Anatoly V. Streltsov
Embry Riddle Aeronautical University, streltsa@erau.edu

Scholarly Commons Citation

Mishin, E. V., & Streltsov, A. V. (2024). Toward the unified theory of SAID-linked subauroral arcs. Journal of Geophysical Research: Space Physics, 129, e2023JA032196. https://doi.org/10.1029/2023JA032196

JGR Space Physics

RESEARCH ARTICLE
10.1029/2023JA032196

Key Points:

- Nightside Stable Auroral Red (SAR) arcs emerge and follow the evolution of the fasttime subauroral ion drifts (SAID) until the ensuing emergence of Strong Thermal Emission Velocity Enhancement (STEVE)
- Density trough formation with the E-region valley initiates the emergence of STEVE and Picket Fence underneath of the precursor SAR arc
- Small-scale parallel electric fields created by the ionospheric feedback instability in the low-density SAID channel make STEVE and Picket Fence

Correspondence to:
E. V. Mishin,
evgeny.mishin@spaceforce.mil;
evlpaem@gmail.com

Citation:
Mishin, E. V., & Streltsov, A. V. (2024). Toward the unified theory of SAID-linked subauroral arcs. *Journal of Geophysical Research: Space Physics*, *129*, e2023JA032196. https://doi.org/10.1029/2023JA032196

Received 17 OCT 2023
Accepted 24 NOV 2023

Author Contributions:
Conceptualization: Evgeny V. Mishin
Data curation: Evgeny V. Mishin
Formal analysis: Evgeny V. Mishin, Anatoly V. Streltsov
Investigation: Evgeny V. Mishin, Anatoly V. Streltsov
Methodology: Evgeny V. Mishin
Software: Anatoly V. Streltsov
Validation: Anatoly V. Streltsov
Writing – original draft: Evgeny V. Mishin, Anatoly V. Streltsov
Writing – review & editing: Evgeny V. Mishin, Anatoly V. Streltsov

Toward the Unified Theory of SAID-Linked Subauroral Arcs

Evgeny V. Mishin[1] **and Anatoly V. Streltsov**[2]

[1]Air Force Research Laboratory, Space Vehicles Directorate, Albuquerque, NM, USA, [2]Department of Physical Sciences, Embry-Riddle Aeronautical University, Daytona Beach, FL, USA

Abstract We present a unified approach to subauroral arcs within intense subauroral ion drifts (SAID), which explains the observed transition of a precursor Stable Auroral Red (SAR) arc into Strong Thermal Emission Velocity Enhancement (STEVE). This approach is based on the short-circuiting concept of fasttime SAID as an integral part of a magnetospheric voltage generator between the innermost boundaries of the freshly injected plasma sheet electrons and ring current ions. Here, enhanced plasma turbulence rapidly heats the bulk plasma and accelerates suprathermal non-Maxwellian "tails." Heat and suprathermal electron transport rapidly elevate the ionospheric electron temperature—the source of a bright SAR arc. Through a substorm, the density altitude profile within the evolving ionospheric SAID channel transforms into a "fresh" F-region trough with the E-region valley. The ionospheric feedback instability within the depleted-density SAID channel generates small-scale, field-aligned currents with parallel electric fields sufficient to produce the suprathermal electron population, exciting the STEVE and Picket Fence emissions. This approach also explains the inner electromagnetic structure of intense SAID, which is consistent with fine optical structures in STEVE and Picket Fence.

1. Introduction

Subvisual Stable Auroral Red (SAR) arcs, typically of ~300–500 Rayleigh (R), at altitudes $h \sim$ 300–400 km are frequently observed in the subauroral ionosphere (see, e.g., Gallardo-Lacourt et al., 2021). The spectrally pure redline ("r") emission at 630 nm via $O(^1D) \rightarrow O(^3P) + h\nu_r$ is consequent to thermal electron excitation of the $O(^1D)$ state with the threshold energy of $\varepsilon_r \approx 1.96$ eV. Quiet time SAR arcs appear inside the ring-current-related ionospheric trough (RIT, e.g., Karpachev, 2021) with elevated F-region electron temperature, $T_e \gtrsim 2{,}500$ K, maintained by the heat flux from the plasmasphere heated by Coulomb collisions with the ring current (RC) ions (e.g., Ihaba et al., 2020; Kozyra et al., 1997). The RIT is adjacent to the equatorward wall of the main ionospheric trough (e.g., Aa et al., 2020) located between the ionospheric footprints of the plasmapause and the electron plasma sheet (PS) (e.g., Heilig et al., 2022; Yizengaw & Moldwin, 2005).

During disturbed conditions, significantly brighter SAR arcs are observed in newly formed troughs with $T_e \gtrsim 3{,}500$ K in enhanced subauroral convection flows (e.g., Baumgardner et al., 2007; Förster et al., 1999; Foster et al., 1994). The disturbed subauroral convection near the local midnight is dominated by narrow, $\Delta_S \lesssim 1°$ in latitude, fast, $v_H \gtrsim 1$ km/s, westward flows—subauroral ion drifts or SAID (Spiro et al., 1979). SAID are driven by meridional (outward/poleward) electric fields, E_Λ, sandwiched between the RC and PS innermost borders (e.g., Horvath & Lovell, 2023; Mishin, 2013, 2023). This region in the plasmasphere exhibits elevated plasma temperature and suprathermal (up to ~300 eV) non-Maxwellian "tails" due to enhanced plasma turbulence (e.g., MS2021a, Figures 8.3–8.4). Henceforth, MS stands for Mishin and Streltsov.

Late in large substorms, east-west-aligned Strong Thermal Emission Velocity Enhancement (STEVE) and Picket Fence arcs appear within intense SAID channels with high velocities, $v_H \gtrsim 4$ km/s, and deep troughs of $n_{min} \sim 10^4$ cm^{-3} with $T_e > 5{,}000$ K at altitudes $h \sim$ 450–800 km (Archer, Gallardo-Lacourt, et al., 2019; Chu et al., 2019; Gallardo-Lacourt et al., 2018; MacDonald et al., 2018; Nishimura et al., 2019). If it appears, Picket Fence lags STEVE (Martinis et al., 2022; Yadav et al., 2021) but can remain after STEVE disappears. Picket Fence arcs reside in the height range of $130 < h_1 < 180$ km and STEVE arcs at $200 < h_2 < 270$ km (Archer, St.-Maurice, et al., 2019; Liang et al., 2019; Martinis et al., 2021). The STEVE purple/mauve color is determined by a 400–800 nm Air Glow Continuum (AGC), while the green- ("g", $O(^1S) \rightarrow O(^1D) + h\nu_g$ at 557.7 nm) and red-line emissions increase just a little (Gillies et al., 2019, 2023; Liang et al., 2019).

STEVE is observed to follow on a precursor SAR arc (e.g., Chu et al., 2019; Gillies et al., 2023; Liang et al., 2019; Martinis et al., 2022, 2021). In particular, the transition of bright SAR arcs into STEVE arcs at lower altitudes was documented (Gillies et al., 2023; Martinis et al., 2022). The SAR arcs, ∼2 and ∼6 kR, were related to intense SAID channels with $V_W \gtrsim 4$ and 5.5 km/s, $T_e \sim 6{,}000$ and 8,000 K, and $n_{min} \sim 3 \times 10^4$ cm^{-3} at ∼450 km, respectively. Notably, about 10 min after the onset of a substorm, Gillies et al. (2023) detected a SAR arc moving southward with the width increasing. After ∼20 min, near the beginning of the substorm recovery, the arc abruptly narrowed and transformed into STEVE/AGC with the redline luminosity nearly doubled and the equatorward motion temporarily stopped. Once the AGC faded away in ∼25 min, a weak SAR arc reappeared. The flow speed and T_e in the SAID/STEVE channel were significantly greater, while the width and n_{min} were much smaller than during the preceding SAR arc (Martinis et al., 2022). Thus, Gillies et al. (2023) assume that the red-into-AGC transition manifests some unknown threshold condition.

Whichever the threshold is, the AGC calls for strongly excited nitrogen molecules, N_2 (Harding et al., 2020; MS2019). Moreover, MS2019 have shown that at $h \lesssim h_2$, where $n_e \le n_e^{(vib)} \approx 10^{-3} N_{N_2}$ (the N_2 density), a non-Maxwellian suprathermal tail is the main excitation source because the N_2 vibrational barrier bites off the thermal electron distribution function (EDF) at $\varepsilon \ge \varepsilon_r$ (e.g., Mishin et al., 2000). This inference is a fortiori valid for the Picket Fence spectrum, which is dominated by the green line and the first positive band $N_2(^1P)$ at ≥650 nm from the $N_2(B^3\Pi_g)$ or $N_2(B)$ state, while lacking the blue-line ("b") emission at 427.8 nm (Mende et al., 2019; Mende & Turner, 2019). That is, an enhanced suprathermal tail extends beyond the $O(^1S)$ and $N_2(B)$ excitation thresholds of $\varepsilon_g \approx 4.2$ eV and $\varepsilon_B \approx 7.35$ eV, respectively, but is cut off at $\varepsilon_b = 18.75$ eV (Mende et al., 2019).

As suprathermal electrons coming from the plasmasphere degrade along the path (e.g., Khazanov et al., 2017), the observations call for a local source of suprathermal electrons. MS2022 attributed the source to parallel electric fields, $\delta E_\parallel$, inherently linked to small-scale, field-aligned currents (FACs), $\delta j_\parallel$, carried by dispersive Alfvén waves generated in the SAID channel by the ionospheric feedback instability (IFI). Note that the linear theory relation for inertial Alfvén waves is $\delta E_\parallel \propto \omega_k \delta j_\parallel / n_e$. As the input for the IFI simulation, MS2022 included a so-called ionospheric "valley" of $n_e^{(v)} \sim 10^3$ cm^{-3} between ≥120 and ≤200 km (Titheridge, 2003) in addition to the F-region trough. A rigorous solution of the Boltzmann kinetic equation with $\delta E_\parallel(h)$ from this simulation gives a local EDF, $F_e(\varepsilon, \delta E_\parallel(h))$, which satisfies the requirements for STEVE above 200 km and Picket Fence beneath. On the other hand, the EDFs obtained in the runs without the valley were insufficient. The MS2022 simulation and similar runs (e.g., Streltsov & Mishin, 2022; henceforth, SM2022) show that the gradient of the Alfvén speed near the valley's upper boundary reflects FACs-carrying Alfvén waves with the reflection coefficient stronger for shorter-scale waves. Thus, the valley works like a lowpass filter, which passes the magnetospheric waves with larger perpendicular wavelengths and reflects short-scale waves.

The most recent observational findings include fine-scale optical structures in STEVE (Nishimura et al., 2023) and the small-scale meridional structure of the electromagnetic field (MS2023) and density trough (Sinevich et al., 2023) within intense SAID, like that linked to STEVE arcs. The MS2023 IFI simulation reproduced in detail the SAID electromagnetic structure, thus validating that the IFI captures the basic physics of the small-scale magnetosphere-ionosphere coupling in SAID events. Given the $\delta E_\parallel - \delta j_\parallel$ intimate relation, it is anticipated that the arc brightness would have a similar small-scale structure. In addition, nonlinear interactions of the IFI-generated Alfvén waves create a series of electrostatic convective cells—small-scale vortices along the channel (e.g., Pokhotelov et al., 2003). Combined with the inner structure across the channel/arc, these would make a 3D optical fine structure in the height range of STEVE and Picket Fence.

As the required magnitudes of $\delta E_\parallel$ are attained in a low-density F region with the valley beneath (MS2022), we suggest that the SAR arc-into-STEVE transition is determined by the formation of such depleted density profile in the evolving ionospheric channel. This assertion is examined below. Section 2 describes the SAID development during substorms with implications for SAR and STEVE/Picket Fence arcs. The IFI simulation in Section 3 reproduces the inner electromagnetic structure of intense SAID with $\delta E_\parallel(h)$ that makes the specific local EDFs required for STEVE and Picket Fence. We show that SAID-related SAR arcs with their ensuing transition into STEVE follow the progress of the SAID channel started as an integral part of a fasttime magnetospheric voltage generator (VG_{FT}) and then evolved under the action of the elevated temperature and strong electric field, depleting the plasma density within the ionospheric counterpart.

2. Substorm SAID: Implications for Subauroral Arcs

Here, we present a scenario of the development of a SAID-linked subauroral arc within a typical SAID channel evolving throughout an isolated substorm. The fast timescale and near-midnight MLT sector point to the earthbound mesoscale plasma flow bursts (MPFs) (Gkioulidou et al., 2014; Horvath & Lovell, 2023; Mishin, 2013; Mishin & Puhl-Quinn, 2007; Nishimura et al., 2022; Z. Wang et al., 2019; W. Wang et al., 2021). SAID are created as an integral part of the VG_{FT} by the short circuiting of earthbound MPFs over the plasmapause (Mishin, 2013, 2023; Mishin & Puhl-Quinn, 2007). As a result, SAID appear in the near midnight plasmasphere interior to L_{min}—the L-shell where the plasma density at the plasmapause exceeds the critical value of $n_p(L_{min}) = n_p^{(min)} \sim 10\,cm^{-3}$. Here, the self-polarization field at the incoming MPF's front is short-circuited by the cold plasma, so that the MPF's electrons stop and form the "fresh" electron PS boundary (hence the auroral boundary). Meanwhile, the demagnetized (Mishin, 2013, Equation 4) hot MPF's ions—the "fresh" RC injection—move further inward until being halted by the emerging SAID electric field, E_Λ. This way, the VG_{FT} is created between the substorm PS and RC innermost boundaries. Its initial east-west dimension of, typically, ~2–3 MLT hours is determined by that of the MPF.

For substorms initiated by intense MPFs (e.g., Fukui et al., 2020; Henderson, 2012; Lyons & Nishimura, 2020; Nishimura et al., 2010), the VG_{FT}/SAID follow hard upon the prebreakup arc brightening (e.g., MS2020, 2021b, Chapter 5.1). That is, the plasmaspheric SAID channel develops shortly after, or concurrently with, the substorm onset. Once formed, it then persists for a few hours. In a quasi-stationary state, the SAID field in the plasmasphere electrostatically maps to the ionospheric counterpart on the RIT's poleward wall (e.g., Anderson et al., 2001; Figueiredo et al., 2004; MS2021a, Figure 8.7) owing to the plasmapause-trough relation (e.g., Heilig et al., 2022; Karpachev, 2021). The plasmapause-SAID relation connects the equatorward/inward motion of SAID (e.g., Figueiredo et al., 2004; Mishin, 2013, Figure 12; Puhl-Quinn et al., 2007, Figure 2) with the inward moving plasmapause (and the electron PS) due to the increasing convection field (e.g., Chen & Wolf, 1972) and SAID-caused erosion (Goldstein et al., 2003).

The freshly injected, hot RC ions have an anisotropic distribution that evolves into a "nose" near the innermost border of the SAID channel, where the hot ion pressure gradient drives the ion diamagnetic (azimuthal) current. In turn, the electron pressure gradient near the plasmapause/PS innermost edge drives the electron diamagnetic currents. Unstable ion distributions and diamagnetic currents generate intense plasma turbulence—the source of the fast bulk plasma heating and acceleration of suprathermal (up to 200–300 eV) tail particles—between the plasmapause and the nose (e.g., Mishin, 2013, 2023; Mishin & Burke, 2005; Mishin & Sotnikov, 2017). This turbulent state remains in place well into the substorm recovery.

Enhanced above $\sim 10^{10}$ eV/cm^2/s heat conduction and suprathermal electron fluxes characteristic of intense SAID elevate T_e—the source of a "fresh" SAR arc in the conjugate topside ionosphere—up to $\gtrsim$5,000 K; theoretically, within a few minutes (e.g., Khazanov, 2011; Rees & Roble, 1975). Thus, the fresh SAR arc would emerge shortly after the substorm onset as a rapid brightening of the pre-substorm SAR arc expanding over the elevated T_e region between the plasmapause and the ion nose (e.g., MS2021a, Figure 8.7). The fresh SAR arc would follow the plasmapause's equatorward motion, like the precursor SAR arcs in the documented transition events. Suprathermal electrons in the topside ionosphere would also excite multiple emission lines, such as reported by Mendillo et al. (2016).

Statistically (e.g., Figueiredo et al., 2004; Karlsson et al., 1998), ionospheric SAID channels observed at earlier times are wider and their peak amplitudes are smaller than at later times. Oksavik et al. (2006) reported on a fast shrinkage of the subauroral backscatter from the SAID region. Figure 1 shows an example of a fast change in the SAID width and peak amplitude in the plasmasphere. It was detected near L = 5.3 and 21.1 MLT during an inner-magnetospheric pass of the Cluster spacecraft at the end of the expansion phase of an individual substorm commencing at ≈12:00 UT on 18 April 2005 (Mishin, 2013). The time lag between the satellites is taken into account. C1/C2/C3 encountered the outer boundary of the channel at the plasmapause at $R_{min} \approx 4.13R_E/4.01R_E/3.99R_E$, with C2/C3 lagging the headmost C1 by 7.0/15.8 min (Mishin, 2013).

Between the C1 and C2 crossings, the outer boundary moved inward by $\approx 0.12R_E$, while a wider electric structure reduced to a typical narrow SAID channel with practically the same cross-channel voltage, that is, ≈8.5 versus ≈8.05 kV. The continual voltage and remarkably alike hot ion distributions agree well with a stationary magnetospheric voltage generator (e.g., Mishin, 2023). Note that the inward motion practically stopped after the

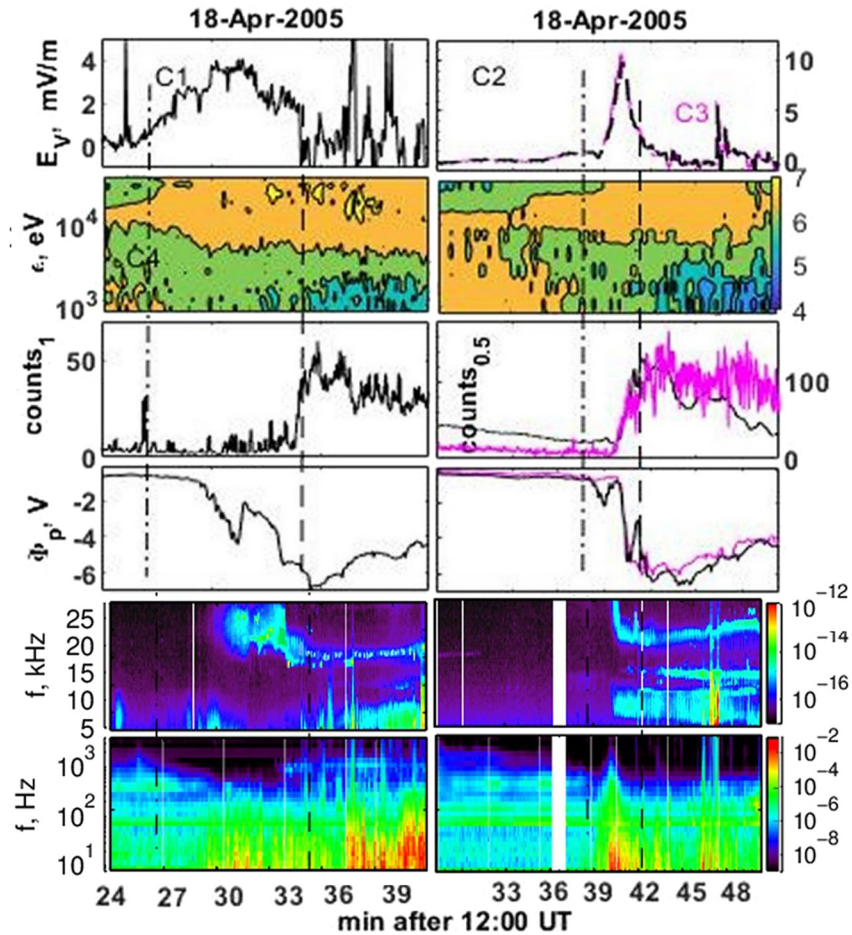

Figure 1. The 18 April 2005 subauroral ion drifts (SAID) event from the Cluster spacecraft. (top row) Outward electric fields from (left) C1 and (right) C2/C3 shown by black/magenta lines; (second row) H^+ differential, $\perp \boldsymbol{B}_0$, number fluxes; (third row) electron counts from C1 (1 keV) and C2/C3 (0.5 keV); (fourth row) floating potentials; and frequency-time spectrograms for the electric field from (fifth row) the C1 and C3 WBD instrument for the electric field in $(V/m)^2/Hz$ and (bottom row) from C4 and C3 STAFF in $(mV/m)^2/Hz$. Color codes in logarithmic scale for the directional differential fluxes and for the wave spectrum are given to the right of the spectrograms. The auroral boundary (the dashed line) is marked by the drop of the background electron counts and the rise of the floating potential. Adapted from Mishin (2013, Figure 12).

channel narrowed and that, as usual, broadband low-frequency waves are seen between the plasmapause and the nose being more enhanced inside the channel. A "thick" upper hybrid (light blue) line indicates the presence of suprathermal electrons in the plasmasphere (Mishin & Burke, 2005).

A similar shrinkage of the channel with the increase of the peak amplitude in the ionospheric SAID is observed in the SAR arc-into-STEVE transition event, along with the decreasing plasma density (Martinis et al., 2022). The latter observation indicates the importance of the trough development within the channel, which will be discussed next.

We define the trough depth as

$$\delta n_{\min}(h) = 1 - n_{\min}(h)/n_0(h) \tag{1}$$

($n_{\min}/n_0$ is the minimum/background plasma density). The ionization balance in the O^+-dominated F region is determined by the recombination of molecular ions NO^+ and O_2^+, created via the charge exchange reactions, $O^+ + X_2 \rightarrow XO^+ + X$ with X = N or O, since the recombination rate of O^+ ions is very small. Accordingly, subauroral ionization troughs have long been explained (e.g., Anderson et al., 1991; Moffett et al., 1998; Pavlov & Foster, 2001; Schunk et al., 1976) through a combination of enhanced charge exchange reactions and plasma outflows due to frictional ion heating. The latter follows the formation of the ionospheric SAID channel, which

takes a number of Alfvén wave bounce periods, typically, $\tau_A^{(I)} \sim 5$ min (see Section 4). Over this time, the charge exchange process due to elevated T_e is the main contributor.

The charge exchange rate of vibrationally excited molecular species increases in the region of elevated T_e (e.g., Moffett et al., 1998; Pavlov, 1996; Pavlov & Foster, 2001). Mishin et al. (2004) numerically simulated subauroral density depletions, $\delta n_{min} \sim 0.8$ or $n_{min} \sim n_0/5 \sim 3 \times 10^4$ cm^{-3}, measured at 850 km and related to elevated $T_e \approx$ 6,000–9,000 K (see MS2021a, Figure 8.9). The vibrational excitation rate, k_{vib}, was calculated with a Maxwellian EDF, $F_M(\varepsilon,T_e)$. The value of T_e at 300 km was taken by a factor of ~2 smaller than at 850 km, likewise the SAID/SAR arc events (Baumgardner et al., 2007; Förster et al., 1999; Foster et al., 1994). Enhanced charge exchange depleted the F_2 peak at 300 (400) km with $n_0 = 3 \times 10^5$ cm^{-3} and T_e = const = 3,500 (4,000) K to $n_{min} \sim (0.5 \rightarrow 0.2) n_0$ in ~10→30 min.

The gain in T_e rapidly decreases below 300 km (e.g., Förster et al., 1999, Figure 5c; Foster et al., 1994, Figure 6b; Liang et al., 2022, Figure 2). Besides, the vibrational barrier cuts off the number of "vibrationally active" tail electrons at $N_{N2} \gtrsim 10^3 n_e$. Thus, little contribution from the vibrational mechanism is anticipated below ~300 km. Yet, a Maxwellian EDF is a valid approximation for $n_e > n_e^{(vib)} \lesssim 3 \times 10^4$ cm^{-3} at >300 km (e.g., MS2019, Figure 4), that is, in the height range of SAR arcs. Here, balancing an external electron-heating source, Q_e, by inelastic losses (see, e.g., MS2021b, Figure 4.3.3) gives an estimate of $T_e \propto Q_e^{-2/5} n_e^{-2/5}$ for $T_e \approx$ 6,000–10^4 K. Higher temperatures lead to higher k_{vib} and a deeper depletion via a positive feedback loop, $\delta T_e \rightarrow \delta n_e \rightarrow \delta T_e$. This effect should increase the depletion rate relative to that in Mishin et al. (2004).

However, at any rate, $n_{min} \gtrsim n_e^{(vib)}$ is expected. As soon as the F_2-peak density reduces and the initial equilibrium breaks down, the surrounding plasma flows into the depleted region like a rarefaction wave propagating away from the peak. A steady-state topside altitude profile can be evaluated assuming diffusive equilibrium in a given temperature profile (Schunk et al., 1976). The O^+ scale height in high temperature events is as large as 400–500 km, so the altitude profile of high T_e troughs is expected to be nearly flat, $\delta n_{min}(h) \approx$ const, from the F_2 region to the top (e.g., Foster et al., 1994, Figure 6c).

Concerning implications for SAR arcs, the rapid increase of the O(^{1}D) thermal excitation rate with T_e overcomes its decrease with the depleted n_e at $T_e \leq$ 15,000 K (e.g., MS2021b, Figure 5.3.12). Thus, the SAR arc brightness would increase with time on the freshly depleted RIT walls (arc flanks) for $n_e > n_e^{(vib)}$. In other words, the arc width would widen (cf. Gillies et al., 2023, Figure 1). Moreover, the arc's poleward side would be brighter because the wave activity is most intense in the turbulent plasmasphere boundary layer (TPBL) near the plasmapause (Mishin et al., 2010; Mishin & Sotnikov, 2017; MS2021a, Figure 8.4), as demonstrated by Figure 1.

As soon as the ionospheric channel is formed, the depletion rate near the peak amplitude upsurges as the ion ohmic heating accelerates charge exchange reactions and ion outflows. For ballpark estimates, a 0.1 V/m electric field (the O^+ drift speed of $v_E \approx 2$ km/s and energy of $\varepsilon_E \approx 0.33$ eV) yields $\delta n_{min} \approx 0.7$ at a 300 km altitude (Schunk et al., 1976). Unlike the T_e-related vibrational mechanism, the electric field acts in the entire flux tube, including the E region. Liang et al. (2021, 2022) simulated the SAID/trough evolution by means of a 2D, time-dependent model. Their model includes the Pedersen transport in addition to the "standard" ohmic heating and vibrational excitation mechanisms, though taking no account of the vibrational barrier. The downward electron heat flux is imposed as the boundary condition at 800 km altitude. The simulations reveal the key role of the ion Pedersen transport in the dynamic variations of the lower ionosphere (<200 km altitude) in intense SAID. In particular, they show a deep F-region trough with strongly elevated T_e (above ~250 km) and T_i (throughout), as well as a valley of $n_e^{(v)} \lesssim 10^3$ cm^{-3} between ≳100 and ≲180 km, for both ultimate SAID drivers, that is, the constant (large-scale) FACs enclosing the channel or the constant voltage.

As expected in the current generator model, the ionospheric electric field increases in unison with the decreasing plasma density with the characteristic time scale of $\tau_n \sim 5$ min (Liang et al., 2022, Figure 4). However, the shrinkage of the channel with the increase of the peak amplitude, such as in Figure 1 and the transition event (Martinis et al., 2022), was not reproduced in the Liang et al. (2021, 2022) simulations. For that, it is necessary to start with the constant voltage magnetospheric generator and then allow for the FACs to maintain the voltage in the depleted plasma (cf. Figueiredo et al., 2004; Karlsson et al., 1998; W. Wang et al., 2021). In any case, the depleted density profile with a valley would be formed.

Next, we simulate the IFI development in intense SAID with the depleted density profile.

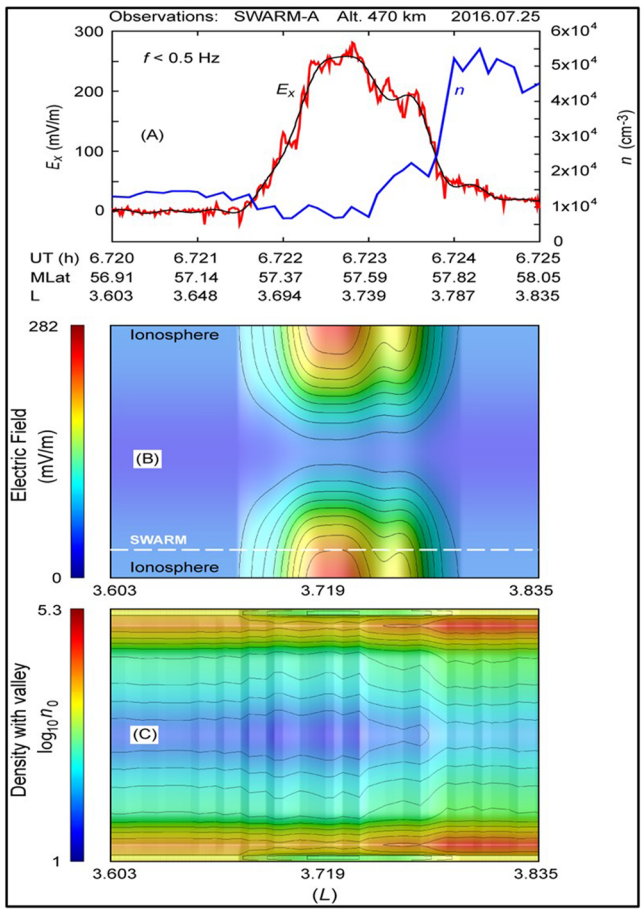

Figure 2. The 25 July 2016 event. (a) The measured (red color, E_Λ) and lowpass filtered (black, $\langle E_\Lambda \rangle$) meridional electric fields and the plasma density (blue) along the Swarm-A pass. The filter cutoff frequency is indicated. $\langle E_\Lambda \rangle$ is the large-scale part of the electric field used to construct the background electric field in the computational domain in frame (b). (c) The spatial distribution of the input background plasma density inside the computational domain. The dashed line marks the "trajectory" of a virtual satellite in the computational domain.

3. IFI Simulation Within Low-Density SAID Channels

The feedback of the variations of the ionospheric plasma density on the FACs' structure and dynamics is an essential element of the magnetosphere-ionosphere coupling (e.g., Streltsov & Mishin, 2018; henceforth, SM2018). The altitude-dependent, ion-neutral collision frequency, $\nu_{in}(h)$, creates a strongly sheared convection flow, which makes short transverse-wavelength, $\lambda_\perp \sim$ 1–10 km, dispersive Alfvén waves carrying small-scale FACs "over-reflect" from the E-region ionosphere (e.g., Trakhtengertz & Feldstein, 1991). For the E-region plasma density of $n_{0E} \leq 10^4$ cm^{-3}, the IFI threshold is only ~0.1 $E_\Lambda \sim$ 20–30 mV/m.

Specifically, we model the meridional electromagnetic structure from Swarm-A in the 25 July 2016 STEVE/SAID event described in detail by MS2023. As shown earlier (e.g., MS2023; SM2022), the input/background plasma density and the electric field are obtained by extrapolating the pertinent data from Swarm-A in Figure 2a to the entire domain. Because large-scale parallel electric fields in SAID are absent, the lowpass filtered electric field, $\langle E_\Lambda \rangle$, is mapped electrostatically. The plasma density is mapped using the formulae and coefficients from SM2018 and SM2022. Here, we assume the plasma density in the ionospheric E region (110 km altitude), $n_{0E} = 2.5 \times 10^3$ cm^{-3}, a depleted F_2 peak at 300 km, $n_{F2} = 3.5 \times 10^4$ cm^{-3}, and $n_{eq} = 10$ cm^{-3} in the equatorial plane. The density in the valley, $n_e^{(vI)}$, between 120 and 150 km altitude is assumed to be 1.25×10^3 cm^{-3}. Figures 2b and 2c show the spatial distributions of the input background electric field and the plasma density inside the computational domain obtained by the extrapolation discussed above.

As in earlier papers (e.g., MS2019; MS2022; MS2023; SM2018; SM2022), a reduced two-fluid MHD model describing dispersive Alfvén waves in low-β plasmas is used. The model consists of the electron parallel momentum equation, the density continuity equation, and the current continuity equation. These equations are solved numerically using the finite-difference-time-domain technique (FDTD) in a two-dimensional computational domain representing an azimuthal slice of the dipole magnetic flux tube (see details in, e.g., SM2022). In the meridional ("x") direction, the domain is bounded by $L = 3.603$ and $L = 3.835$ magnetic shells according to the observed SAID dimension along the satellite trajectory. In the direction along the ambient magnetic field ("z"), the domain is bounded by the ionosphere at altitude 110 km.

In the model, we set the electron temperature, T_e, proportional to $1/n_e$ so that $\nabla_\parallel p_e = \nabla_\parallel (n_e T_e) = 0$. The maximum value of T_e in the disturbed equatorial magnetosphere is set to 100 eV. In this case, the maximum value of T_e in the E-region and in the valley is about 4,600 and 9,200 K, respectively. The latter is close to the observed values in STEVE events. However, note that the input values of T_e have an insignificant effect on the IFI development, while T_i is more essential. Indeed, T_i determines the ion mobility and hence the Pedersen conductivity, σ_P, which controls the FACs closure by the Pedersen current in the ionosphere. As in the E region $\sigma_P \sim n_i/\nu_{in}(T_i)$, ohmic heating of the ionospheric ions reduces the Pedersen conductivity and thus the IFI-generated FACs. This mechanism can lead to instability saturation. The self-consistent treatment of the IFI development with the ion ohmic heating included is a formidable task for future research.

Simulation starts from the current-free equilibrium state. The IFI develops from numerical noise, which can be interpreted as random thermal fluctuations of the background plasma. Figure 3a shows the temporal dynamics of the meridional electric field taken from the computational domain at the Swarm-A altitude. The IFI-generated waves become noticeable after ~200 s in simulation. The waves are amplified until saturation at about 270 s (marked with the arrow). Figure 3b shows the saturated electric field (red line), E_{sim}, and the plasma density from

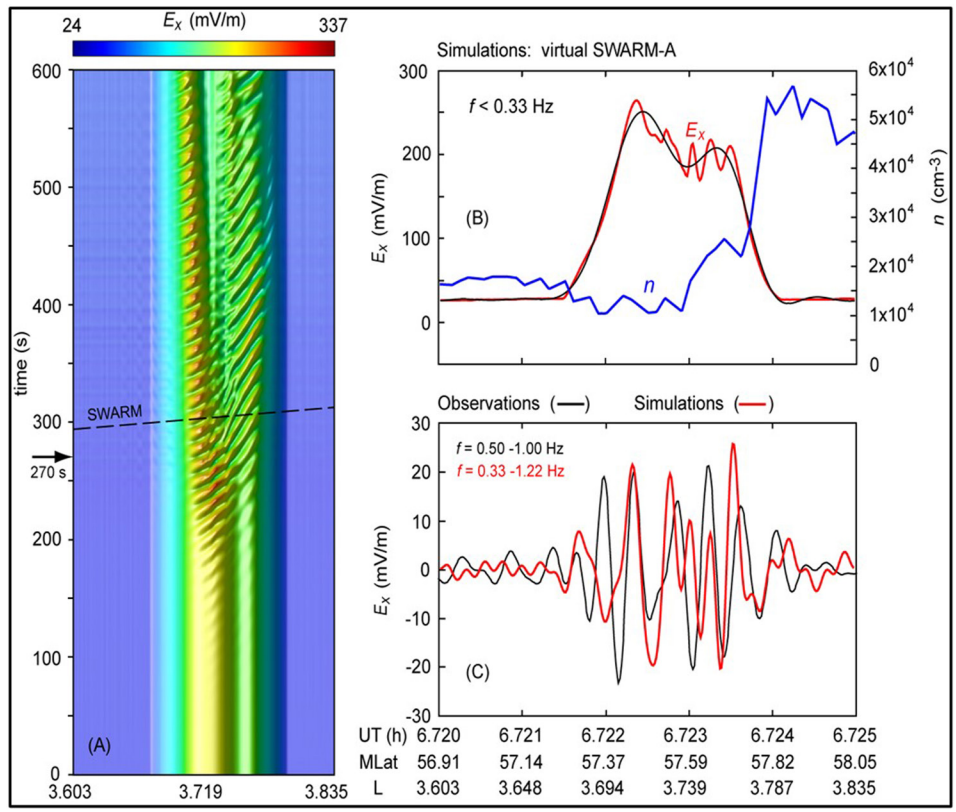

Figure 3. The ionospheric feedback instability (IFI) simulation of the 25 July 2016 event. (a) The temporal dynamics and spatial structure of the simulated meridional electric field taken from the computational domain at the altitude of the SWARM-A satellite. (b) The saturated electric field (the red curve) and its low frequency ($f < 0.33$ Hz) part (black). The blue curve shows the plasma density along the virtual satellite trajectory. (c) The observed $E_\perp$ in the frequency range 0.5–1.0 Hz (black), and the simulated $E_\perp$ in the frequency range 0.33–1.22 Hz (red).

a virtual satellite "flying" through the computational domain along the trajectory corresponding to Swarm-A (the dashed line in Figure 3a). Finally, Figure 3c shows the observed $E_\perp$ in the frequency range 0.5–1.0 Hz (with black line), and the simulated $E_\perp$ in the frequency range 0.33–1.22 Hz (red line) along the trajectory of the virtual Swarm satellite.

As illustrated by Figure 3, the simulation reproduces the large- and small-scale features in good, quantitative detail. In other words, the IFI model captures the underlying physics of the magnetosphere-ionosphere coupling in the STEVE/SAID channel. Further, Figures 4a–4d show snapshots of $\delta j_\parallel$ and $\delta E_\parallel$ taken from the simulation with (without) the valley after saturation at 270 s (at 600 s). Figure 4e shows the corresponding plasma density profiles along the ambient magnetic field between 118 and 400 km altitude.

MS2022 evaluated the effect of $\delta E_\parallel$ with the aid of the power distribution over inelastic processes (the energy balance) from a numerical solution of the Boltzmann kinetic equation with the input values of $\delta E_\parallel / N_n \equiv \tilde{E}$ from 1 to 200 Td (Dyatko et al., 1989). Here, the Townsend unit 1 [Td] = 10^{-17} [V cm^2] and the neutral density, N_n, total the densities of N_2, O, and O_2. For example, for $N_n = 10^{12}$ cm^{-3} at ~120 km, $\tilde{E} = 1$ Td yields $\delta E_\parallel = 1$ [mV/m]. For the composition typical of ~120 km (e.g., Picone et al., 2002), Figure 3c in MS2022 shows that the power, P_V, spent on excitation of vibrational levels of the ground state $N_2\left(X^1\Sigma_g^+\right)$ exceeds 50% at $\tilde{E} > \tilde{E}_V \approx 5$ Td and reaches a broad maximum ~90% at $\tilde{E}_V^{(max)} \sim 20$ Td. Excitation of the N_2 electronic levels takes away the power $P_A \approx 3\%$ (mainly the $A^3\Sigma_u^+$ state) at $\tilde{E} = \tilde{E}_A \approx 40$ Td and $P_\Sigma \approx 50\%$ at $\tilde{E}_\Sigma \approx 100$ Td, while the rest goes to vibrational excitation. About 30% of P_Σ goes into the triplet, $A^3\Sigma_u^+$ ("A"), $B^3\Pi_g$ ("B"), and $C^3\Pi_u$ ("C"), and about 10% goes mainly to $O(^1D)$ and $O(^1S)$. The ionization of N_2 begins at $\tilde{E} = \tilde{E}_{ion} \approx 90$ Td and at $\tilde{E}_\Sigma$ amounts to $P_{ion} \sim 2\%$.

At $\tilde{E}_{ion} < \tilde{E} \le \tilde{E}_\Sigma$, the suprathermal tail is confined within the energy range of ≈3.5 eV < $\varepsilon \le \varepsilon_b$ needed for Picket Fence, while the AGC requires roughly $\tilde{E}_A \le \tilde{E} < \tilde{E}_{ion}$. Figure 5 shows the simulated magnitudes, $|\delta E_\parallel|$,

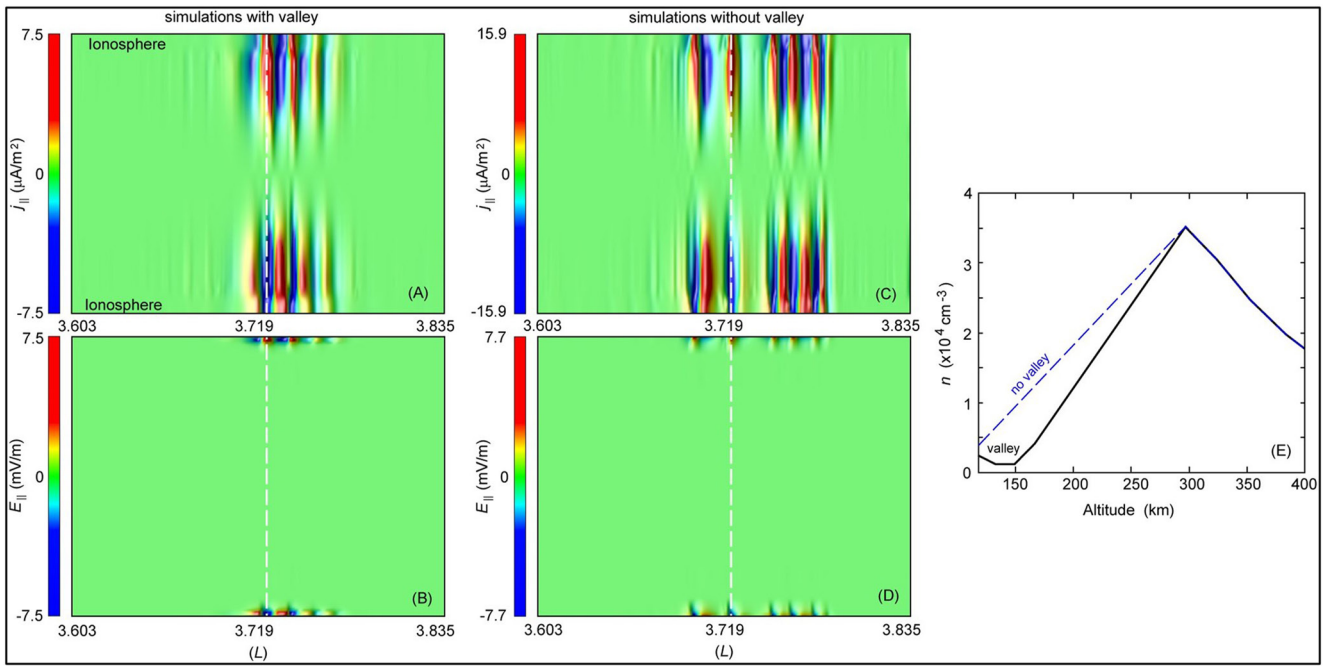

Figure 4. Snapshots of the saturated field-aligned current density, $\delta j_{||}$, and $\delta E_{||}$ in the simulation domain: (a, b) with and (c, d) without the ionospheric valley. (e) The plasma density variation along the ambient magnetic field between 118 and 400 km altitudes with (black solid lines) and without (blue dashed) the valley, as taken along the white dashed line in frames (a, b) and (c, d), respectively.

with (denoted by "vI") and without ("I") the valley from Figure 4 together with altitude profiles of the critical fields, $\delta E_{||}^{(z)} = N_n \cdot \tilde{E}_z$ ("z" stands for "A", etc.), calculated with the midlatitude neutral density model (Picone et al., 2002) for 25 July 2016 increased by a factor of 1.5. Shown for comparison are $|\delta E_{||}|$ simulated for the same input values of n_{0E}, n_{F2}, $n_e^{(vI)}$, and n_{eq} but with a made-up valley extended between 120 and 200 km ("vII"), as well as for a made-up "pre-SAID" background ionosphere ("b") with $n_{F2} = 1.5 \times 10^5$ cm^{-3} and $n_{0E} = 10^4$ cm^{-3}, that is, without the valley and F-region trough.

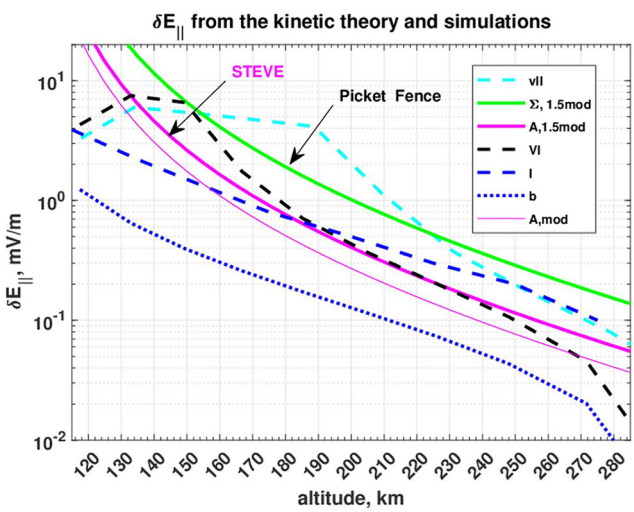

Figure 5. $\delta E_{||}^{(\Sigma)}$ (the green solid line) and $\delta E_{||}^{(A)}$ (thick magenta) calculated with the increased model neutral density and $\delta E_{||}^{(A)}$ (thin magenta) calculated with the model neutral density. The simulated field amplitudes, $|\delta E_{||}|$, for the trough without the ionospheric valley (blue dashed), with the valley I (black dashed), and the extended valley II (cyan dashed), as well as for the background F region (blue dotted), as indicated.

Figure 5 shows that the simulation for the depleted F region with the valley I at 120–150 km produces $|\delta E_{||}|$, satisfying the conditions for both Picket Fence at altitudes ~140–160 km and STEVE below ~250 km. For the depleted F-region trough but without the valley, only STEVE can be excited within the channel. Therefore, shortly after the density height profile within the channel evolves accordingly, STEVE (and Picket Fence) would appear beneath the precursor SAR arc's poleward side. The results strongly depend on the features of the density profile, as illustrated by the simulations for the made-up profiles of the extended valley II and background F region. In the former case, the Picket Fence threshold is exceeded between ~150 and 230 km and that for STEVE between ~240 and 290 km, while in the latter case $|\delta E_{||}|$ is well below the STEVE (and a fortiori Picket Fence) threshold for the model neutral density.

Note that we use the increased model neutral density due to the well-known fact that, along with the density decrease and ion outflows, enhanced ohmic heating results in upwelling in the atmosphere. With the SAID/STEVE parameters, the enrichment of the STEVE region by molecular components should be significant. Indeed, Millward et al. (1993) have calculated that the neutral density at altitudes 300–400 km triples in about 10 min after a 0.2 V/m electric field (v_H ~ 4 km/s) is imposed. This agrees well with fast upwelling caused by a substorm-related ion drift surge of v_H ~ 5 km/s

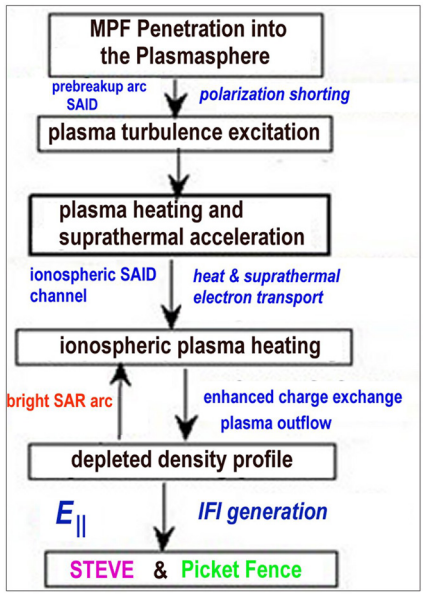

Figure 6. Block diagram showing a scenario of subauroral ion drifts-related Stable Auroral Red and Strong Thermal Emission Velocity Enhancement/ Picket Fence arcs for mesoscale plasma flow bursts-initiated substorms. Denotations on the left (right) side indicate the basic observables (processes).

observed by a tristatic Fabry-Perot interferometer system and the EISCAT UHF radar near a 240 km altitude (Aruliah et al., 2005). Similarly, CHAMP detected an almost doubled mass density at an altitude of ∼400 km in the flow channel of $v_H \geq 3$ km/s in ∼30 min after the storm commencement (Mishin et al., 2007). As, in reality, the gas density increases non-uniformly, mostly in the F region, the $\delta E_{\parallel}^{(\Sigma,A)}$ plots in Figure 5 should be considered only as an illustration.

Figure 6 depicts the overall scenario of the development of SAID-related subauroral arcs during MPFs-initiated substorms (cf. MS2021a, Figure 8.1).

4. Discussion

The Liang et al. (2021, 2022) and the IFI simulations give the timing of the depleted density profile and the IFI of the same timescale, $\tau_n \sim \tau_{IFI} \sim 5$ min. That is, the total time after the ionospheric channel is created is of $\tau_{dn} \sim \tau_A^{(I)} + \tau_n \sim 10$ min. This short timescale contradicts the statistics that STEVE is the substorm recovery feature. However, recall that these simulations, as typical, imply unmoving ionospheric SAID channels. This assumption contradicts the observed inward (equatorward) motion of the channels in the magnetosphere (ionosphere) during the substorm expansion phase. Note also that STEVE arcs appear during strong substorms (e.g., Nishimura et al., 2023, 2022), with the rapidly expanding auroral zone. Furthermore, the shrinkage events in Figure 1 and during the SAR arc-into-STEVE transition occurred near the beginning of the substorm recovery when the auroral expansion has slowed and eventually stopped. This observation allows us to explain the apparent contradiction as follows. Let us assume that the equatorward speed, U_{eq}, exceeds the critical value of $U_S \sim \Delta_S/\tau_{dn} \lesssim 0.1°$/min $\lesssim 0.25$ km/s, so that the depletion process and the IFI are hampered until the substorm expansion slows down.

Figure 5 illustrates that in addition to a "fresh" F-region trough, which facilitates STEVE, a deep valley beneath is needed for Picket Fence. Moreover, as shown by additional simulations, when the E region is depleted but the F region is still dense, the large gradient of the Alfvén speed near the valley's upper boundary reflects small-scale, mostly unstable Alfvén waves, hereby inhibiting the IFI development. These results allow us to understand why STEVE appears ahead of Picket Fence. As discussed in Section 2, the electron heating above ∼250 km occurs in the whole region between the plasmapause and the RC innermost boundary. The heating time is short relative to the transit time of the equatorward moving plasmaspheric source (manifested by the SAR arc motion). That means that elevated T_e persists, and thus the vibrational mechanism depletes plasma in the moving F region with a broad SAR arc. As soon as the ionospheric SAID channel is formed, the strong electric field facilitates the depletion process and the IFI development within the shrinking SAID channel at the poleward side of the SAR arc. Here, the threshold for STEVE can be reached in the already pre-depleted F region prior to that for Picket Fence beneath.

The depletion process is concurrent with the increase of the vibrational barrier in the F region due to atmospheric upwelling. The latter would hinder thermal excitation in the lower, $\gtrsim$300 km, most intense segment of the precursor SAR arc, thereby making it dimmer or vanishing. The continuing upwelling could eventually increase the neutral density and thus the STEVE threshold at ∼200 km (see Figure 5), hereby quenching STEVE. Yet, Picket Fence could remain because the upwelling effect in the valley is less significant than in the STEVE altitude range. As discussed by MS2023, the structure of $\delta E_{\parallel}$ combined with electrostatic convective cells consequent to a parametric coupling of the IFI-generated Alfvén waves would make a 3D, fine-scale optical structure of STEVE and Picket Fence. Given the irregular structure of the density trough (Sinevich et al., 2023), the SAR arc might also exhibit dim, fine-scale structures.

The effect of the depleted ionospheric density can be considered in a more general context as follows. The transient response of the ionosphere to magnetospheric stresses is determined by the development of the ionospheric currents that close the magnetospheric FACs carried by Alfvén waves from the magnetosphere. They provide a $\mathbf{J} \times \mathbf{B}$ force pulling the ionospheric plasma along the magnetospheric driving force. The ionosphere adds a

resistivity in oscillating electrical circuits, which causes the wave damping via ohmic heating. Specifically, the ionospheric response is determined by the Pedersen, Σ_P, and Alfvén wave, $\Sigma_A = 1/\mu_0 V_A$, conductances through the reflection coefficient of Alfvén waves (e.g., Glassmeier, 1984)

$$R_A = \frac{\Sigma_A - \Sigma_P}{\Sigma_A + \Sigma_P} \approx \begin{cases} -1 \text{ at } \Sigma_P \gg \Sigma_A \\ +1 \text{ at } \Sigma_P \ll \Sigma_A \end{cases} \quad (2)$$

The resulting FAC is given by

$$j_\parallel^{(\infty)} = j_{\parallel i}(1 - R_A)/(1 + R_A) \quad (3)$$

As $j_\parallel^{(\infty)} \to \infty$ for a perfect conductor at $\Sigma_P \gg \Sigma_A$, the ionosphere is "instantly" pulled along the magnetospheric flow, viz., the ionospheric flow channel is "instantly" formed. In a real world, it takes several Alfvén wave bounces, $\tau_A^{(I)}$. On the other hand, as expected from general considerations, the incident waves do not affect the insulator as $j_\parallel^{(\infty)}$ tends to zero and so do the ionospheric currents. That is, the ionosphere is "disconnected" from the magnetospheric driver. For $\Sigma_P \ll \Sigma_A$, one gets $j_\parallel^{(\infty)}/j_{\parallel i} \sim \Sigma_P/\Sigma_A \ll 1$, so the ionospheric flow is lagging the magnetospheric flow, viz., the formation of the ionospheric channel is retarded. As Σ_P decreases faster with the density depletion than Σ_A in the ionosphere, the depleted density profile makes the ionosphere more resistive. The latter is also true for the increasing ion temperature in the E region where $\sigma_P \propto n_i/\nu_{in}(T_i)$. Both these effects during the E-region modification inside the channel make the ionosphere less responsive to magnetospheric changes and, most importantly, inhibit the IFI development when Σ_P drops well below Σ_A. The latter would quench STEVE and Picket Fence, thus leaving the SAR arc alone with the brightness fading out following the plasmaspheric turbulence.

5. Conclusions

The short circuit scenario of the fasttime magnetospheric voltage generator coupled with the ionospheric feedback mechanism predicts the following features of SAID-linked subauroral arcs during substorms:

I. SAR arcs
   a) commence in both hemispheres above ~300–350 km shortly after the substorm onset as a sudden intensification and expansion of the pre-substorm SAR arc between the plasmapause and the RC innermost edge;
   b) move equatorward, broaden, and brighten up, especially at the poleward side, during the substorm expansion phase;
   c) exhibit additional emission lines, most likely, the green line on top;
   d) get dimmer or disappear concurrent with the emerging STEVE, and
   e) contain weak optical structures.

II. STEVE and Picket Fence
   a) result from a specific local EDF produced by small-scale parallel electric fields, $\delta E_\parallel$, generated by the IFI together with small-scale FACs, $\delta j_\parallel$, in the depleted SAID channel;
   b) are located underneath the precursor SAR arc's poleward side;
   c) emerge within the channel shortly after its equatorward motion slows down at the end of the expansion phase;
   d) follow the shrinkage of the channel and increasing peak amplitude caused by the plasma density depletion in accord with a constant magnetospheric voltage generator; and
   e) exhibit fine-scale optical structures resulting from the IFI-generated $\delta E_\parallel$ structures.

III. STEVE
   a) appears prior to Picket Fence beneath, and
   b) is quenched by the atmospheric upwelling and the E-region modification.

Most of these predictions (a–d and g–k) do agree with the features found either in the SAR arc-into-STEVE transition events (Gillies et al., 2023; Martinis et al., 2022) or other SAID, STEVE, and SAR arc events (Chu et al., 2019; Liang et al., 2019; Martinis et al., 2021; MS2023; Nishimura et al., 2023; Sinevich et al., 2023). However, to verify small-scale, optical structures in SAR arcs and $\delta E_\parallel$ in STEVE/Picket Fence, as well as the

atmospheric upwelling effect, additional in situ and ground-based observations with high temporal and spatial resolution in the F and E regions are necessary.

Data Availability Statement

The Swarm data used in this study were obtained at https://swarm-diss.eo.esa.int/#swarm/ as daily CDF files. The code used in the simulations, data files used to run the code, and the results from the simulation shown in Figures 2–4 are available from https://doi.org/10.6084/m9.figshare.24227743.

Acknowledgments
E.V.M. and A.V.S. acknowledge support by the Air Force Office of Scientific Research LRIR 22RVCOR011 and FA9550-23-1-0689. Approved for public release; distribution is unlimited. Public Affairs release approval #AFRL-2023-5076. The views expressed are those of the authors and do not reflect the official guidance or position of the United States Government, the Department of Defense, or of the United States Air Force. This paper was under review when Gasque et al. (2023) reported on the picket fence spectrum calculated from a numerical solution of the Boltzmann kinetic equation with an imposed parallel electric field. Their results are consistent with those of MS2022 used in our work.

References

Aa, E., Zou, S., Erickson, P. J., Zhang, S.-R., & Liu, S. (2020). Statistical analysis of the main ionospheric trough using Swarm in situ measurements. *Journal of Geophysical Research: Space Physics*, *125*(3), e2019JA027583. https://doi.org/10.1029/2019JA027583

Anderson, P., Carpenter, D., Tsuruda, K., Mukai, T., & Rich, F. (2001). Multisatellite observations of rapid subauroral ion drifts (SAID). *Journal of Geophysical Research*, *106*(A12), 29585–29599. https://doi.org/10.1029/2001JA000128

Anderson, P., Heelis, R., & Hanson, W. (1991). The ionospheric signatures of rapid subauroral ion drifts. *Journal of Geophysical Research*, *96*, 5785.

Archer, W., Gallardo-Lacourt, B., Perry, G., St.-Maurice, J.-P., Buchert, S., & Donovan, E. (2019). STEVE: The optical signature of intense subauroral ion drifts. *Geophysical Research Letters*, *46*(12), 6279–6286. https://doi.org/10.1029/2019GL082687

Archer, W., St.-Maurice, J. P., Gallardo-Lacourt, B., Perry, G., Cully, C., Donovan, E., et al. (2019). The vertical distribution of the optical emissions of a STEVE and Picket Fence event. *Geophysical Research Letters*, *46*(19), 10719–10725. https://doi.org/10.1029/2019GL084473

Aruliah, A., Griffin, E., Aylward, A., Ford, E., Kosch, M., Davis, C., et al. (2005). First direct evidence of meso-scale variability on ion-neutral dynamics using co-located tristatic FPIs and EISCAT radar in Northern Scandinavia. *Annales Geophysicae*, *23*(1), 147–162. https://doi.org/10.5194/angeo-23-147-2005

Baumgardner, J., Wroten, J., Semeter, J., Kozyra, J., Buonsanto, M., Erickson, P., & Mendillo, M. (2007). A very bright SAR arc: Implications for extreme magnetosphere-ionosphere coupling. *Annales Geophysicae*, *25*(12), 2593–2608. https://doi.org/10.5194/angeo-25-2593-2007

Chen, A., & Wolf, R. (1972). Effect on the plasmasphere of a time-varying convection electric field. *Planetary and Space Science*, *20*, 483–509.

Chu, X., Malaspina, D., Gallardo-Lacourt, B., Liang, J., Andersson, L., Ma, Q., et al. (2019). Identifying STEVE's magnetospheric driver using conjugate observations in the magnetosphere and on the ground. *Geophysical Research Letters*, *46*(22), 12665–12674. https://doi.org/10.1029/2019GL082789

Dyatko, N., Kochetov, I., Mishin, E., & Telegin, V. (1989). The kinetics of electrons in a weakly ionized ionospheric plasma. *Geomagnetizm i Aeronomiia, English Translation*, *29*, 241–245.

Figueiredo, S., Karlsson, E., & Marklund, G. (2004). Investigation of subauroral ion drifts and related field-aligned currents and ionospheric Pedersen conductivity distribution. *Annales Geophysicae*, *22*(3), 923–934. https://doi.org/10.5194/angeo-22-923-2004

Förster, M., Foster, J., Smilauer, J., Kudela, K., & Mikhailov, A. (1999). Simultaneous measurements from the Millstone Hill radar and the Active satellite during the SAID/SAR arc event of the March 1990 CEDAR storm. *Annales Geophysicae*, *17*(3), 389–404. https://doi.org/10.1007/s00585-999-0389-6

Foster, J., Buonsanto, M., Mendillo, M., Notingham, D., Rich, F., & Denig, W. (1994). Coordinated stable auroral red arc observations: Relationship to plasma convection. *Journal of Geophysical Research*, *99*(A6), 11429–11439. https://doi.org/10.1029/93ja03140

Fukui, K., Miyashita, Y., Machida, S., Miyoshi, Y., Ieda, A., Nishimura, Y., & Angelopoulos, V. (2020). A statistical study of near-Earth magnetotail evolution during pseudosubstorms and substorms with THEMIS data. *Journal of Geophysical Research: Space Physics*, *125*(1), e2019JA026642. https://doi.org/10.1029/2019JA026642

Gallardo-Lacourt, B., Frey, H. U., & Martinis, C. (2021). Proton aurora and optical emissions in the subauroral region. *Space Science Reviews*, *217*(1), 10. https://doi.org/10.1007/s11214-020-00776-6

Gallardo-Lacourt, B., Nishimura, Y., Donovan, E., Gillies, D., Perry, G., Archer, W., et al. (2018). A statistical analysis of STEVE. *Journal of Geophysical Research: Space Physics*, *123*, 9893–9905. https://doi.org/10.1029/2018ja025368

Gasque, L. C., Janalizadeh, R., Harding, B. J., Yonker, J. D., & Gillies, D. M. (2023). It's not easy being green: Kinetic modeling of the emission spectrum observed in STEVE's picket fence. *Geophysical Research Letters*, *50*, e2023GL106073. https://doi.org/10.1029/2023GL106073

Gillies, D., Donovan, E., Hampton, D., Liang, J., Connors, M., Nishimura, Y., et al. (2019). First observations from the TREx spectrograph: The optical spectrum of STEVE and the Picket Fence phenomena. *Geophysical Research Letters*, *46*(13), 7207–7213. https://doi.org/10.1029/2019GL083272

Gillies, D. M., Liang, J., Gallardo-Lacourt, B., & Donovan, E. (2023). New insight into the transition from a SAR arc to STEVE. *Geophysical Research Letters*, *50*(6), e2022GL101205. https://doi.org/10.1029/2022GL101205

Gkioulidou, M., Ukhorskiy, A. Y., Mitchell, D. G., Sotirelis, T., Mauk, B. H., & Lanzerotti, L. J. (2014). The role of small-scale ion injections in the buildup of Earth's ring current pressure: Van Allen Probes observations of the 17 March 2013 storm. *Journal of Geophysical Research: Space Physics*, *119*(9), 7327–7342. https://doi.org/10.1002/2014JA020096

Glassmeier, K.-H. (1984). On the influence of ionospheres with non-uniform conductivity distribution on hydromagnetic waves. *Journal of Geophysics*, *54*, 125–137.

Goldstein, J., Sandel, B., Hairston, M., & Reiff, P. (2003). Control of plasmaspheric dynamics by both convection and subauroral polarization stream. *Geophysical Research Letters*, *30*(24), 2243–2246. https://doi.org/10.1029/2003GL018390

Harding, B., Mende, S., Triplett, C., & Wu, Y. J. (2020). A mechanism for the STEVE continuum emission. *Geophysical Research Letters*, *47*(7), e2020GL087102. https://doi.org/10.1029/2020GL087102

Heilig, B., Stolle, C., Kervalishvili, G., Rauberg, J., Miyoshi, Y., Tsuchiya, F., et al. (2022). Relation of the plasmapause to the midlatitude ionospheric trough, the sub-auroral temperature enhancement, and the distribution of small-scale field aligned currents as observed in the magnetosphere by THEMIS, RBSP, and Arase, and in the topside ionosphere by Swarm. *Journal of Geophysical Research: Space Physics*, *127*(3), e2021JA029646. https://doi.org/10.1029/2021JA029646

Henderson, M. (2012). Auroral substorms, poleward boundary activations, auroral streamers, omega bands, and onset precursor activity. In A. Keiling, E. Donovan, F. Bagenal, & T. Karlsson (Eds.), *Auroral phenomenology and magnetospheric processes: Earth and other planets*. https://doi.org/10.1029/2011GM001165

Horvath, I., & Lovell, B. (2023). Antisunward streaming westward sub-auroral ion drifts (SAID) developed in the postmidnight (1–4) magnetic local time sector during 2013. *Journal of Geophysical Research: Space Physics*, *128*(9), e2023JA031677. https://doi.org/10.1029/2023JA031677

Inaba, Y., Shiokawa, K., Oyama, S.-i., Otsuka, Y., Oksanen, A., Shinbori, A., et al. (2020). Plasma and field observations in the magnetospheric source region of a stable auroral red (SAR) arc by the Arase satellite on 28 March 2017. *Journal of Geophysical Research: Space Physics*, *125*(10), e2020JA028068. https://doi.org/10.1029/2020JA028068

Karlsson, T., Marklund, G. T., Blomberg, L. G., & Mlkki, A. (1998). Subauroral electric fields observed by the Freja satellite: A statistical study. *Journal of Geophysical Research*, *103*(A3), 4327–4341. https://doi.org/10.1029/97ja00333

Karpachev, A. (2021). Statistical analysis of ring ionospheric trough characteristics. *Journal of Geophysical Research: Space Physics*, *126*(10), e2021JA029613. https://doi.org/10.1029/2021JA029613

Khazanov, G. (2011). *Kinetic theory of inner magnetospheric plasma*. Springer.

Khazanov, G., Sibeck, D., & Zesta, E. (2017). Major pathways to electron distribution function formation in regions of diffuse aurora. *Journal of Geophysical Research: Space Physics*, *122*(4), 4251–4265. https://doi.org/10.1002/2017JA023956

Kozyra, J. U., Nagy, A. F., & Slater, D. W. (1997). High-altitude energy source(s) for stable auroral red arcs. *Reviews of Geophysics*, *35*(2), 155–190. https://doi.org/10.1029/96rg03194

Liang, J., Donovan, E., Connors, M., Gillies, D., St-Maurice, J. P., Jackel, B., et al. (2019). Optical spectra and emission altitudes of double-layer STEVE: A case study. *Geophysical Research Letters*, *46*(23), 13630–13639. https://doi.org/10.1029/2019GL085639

Liang, J., St-Maurice, J. P., & Donovan, E. (2021). A time-dependent two-dimensional model simulation of lower ionospheric variations under intense SAID. *Journal of Geophysical Research: Space Physics*, *126*(12), e2021JA029756. https://doi.org/10.1029/2021JA029756

Liang, J., St-Maurice, J.-P., & Donovan, E. F. (2022). Model simulation of SAID intensification in the ionosphere under a current generator: The role of ion Pedersen transport. *Journal of Geophysical Research: Space Physics*, *127*(11), e2022JA030960. https://doi.org/10.1029/2022JA030960

Lyons, L., & Nishimura, Y. (2020). Substorm onset and development: The crucial role of flow channels. *Journal of Atmospheric and Solar-Terrestial Physics*, *211*, 105474. https://doi.org/10.1016/j.jastp.2020.105474

MacDonald, E., Donovan, E., Nishimura, Y., Case, N., Gillies, D. M., Gallardo-Lacourt, B., et al. (2018). New science in plain sight: Citizen scientists lead to the discovery of optical structure in the upper atmosphere. *Science Advances*, *4*(3), eaaq0030. https://doi.org/10.1126/sciadv.aaq0030

Martinis, C., Griffin, I., Gallardo-Lacourt, B., Wroten, J., Nishimura, Y., Baumgardner, J., & Knudsen, D. J. (2022). Rainbow of the night: First direct observation of a SAR arc evolving into STEVE. *Geophysical Research Letters*, *49*(11), e2022GL098511. https://doi.org/10.1029/2022gl098511

Martinis, C., Nishimura, Y., Wroten, J., Bhatt, A., Dyer, A., Baumgardner, J., & Gallardo-Lacourt, B. (2021). First simultaneous observation of STEVE and SAR arc combining data from citizen scientists, 630.0 nm all-sky images, and satellites. *Geophysical Research Letters*, *48*(8), e2020GL092169. https://doi.org/10.1029/2020GL092169

Mende, S. B., Harding, B. J., & Turner, C. (2019). Subauroral green STEVE arcs: Evidence for low-energy excitation. *Geophysical Research Letters*, *46*, 14256–14262. https://doi.org/10.1029/2019GL086145

Mende, S. B., & Turner, C. (2019). Color ratios of subauroral (STEVE) arcs. *Journal of Geophysical Research: Space Physics*, *124*(7), 5945–5955. https://doi.org/10.1029/2019JA026851

Mendillo, M., Finan, R., Baumgardner, J., Wroten, J., Martinis, C., & Casillas, M. (2016). A stable auroral red (SAR) arc with multiple emission features. *Journal of Geophysical Research: Space Physics*, *121*(10), 10564–10577. https://doi.org/10.1002/2016JA023258

Millward, G., Quegan, S., Moffett, R., Fuller-Rowell, T., & Rees, D. (1993). A modelling study of the coupled ionospheric-thermospheric response to an enhanced high-latitude electric field event. *Planetary and Space Science*, *41*(1), 45–56. https://doi.org/10.1016/0032-0633(93)90016-u

Mishin, E. (2013). Interaction of substorm injections with the subauroral geospace: 1. Multispacecraft observations of SAID. *Journal of Geophysical Research: Space Physics*, *118*(9), 5782–5796. https://doi.org/10.1002/jgra.50548

Mishin, E. (2023). The evolving paradigm of the subauroral geospace. *Frontiers in Astronomy and Space Science*, *10*, 1118758. https://doi.org/10.3389/fspas.2023.1118758

Mishin, E., & Burke, W. (2005). Stormtime coupling of the ring current, plasmasphere and topside ionosphere: Electromagnetic and plasma disturbances. *Journal of Geophysical Research*, *110*(A7), A07209. https://doi.org/10.1029/2005JA011021

Mishin, E., Burke, W., & Viggiano, A. (2004). Stormtime subauroral density troughs: Ion-molecule kinetic effects. *Journal of Geophysical Research*, *109*(A10), A10301. https://doi.org/10.1029/2004JA010438

Mishin, E., Carlson, H., & Hagfors, T. (2000). On the electron distribution function in the F region and airglow enhancements during HF modification experiments. *Geophysical Research Letters*, *27*(18), 2857–2860. https://doi.org/10.1029/2000gl000075

Mishin, E., Marcos, F., Burke, W., Cooke, D., Roth, C., & Petrov, V. (2007). Prompt thermospheric response to the 6 November 2001 magnetic storm. *Journal of Geophysical Research*, *112*(A5), A05313. https://doi.org/10.1029/2006ja011783

Mishin, E., & Puhl-Quinn, P. (2007). SAID: Plasmaspheric short circuit of substorm injections. *Geophysical Research Letters*, *34*(24), L24101. https://doi.org/10.1029/2007GL031925

Mishin, E., Puhl-Quinn, P., & Santolik, O. (2010). SAID: A turbulent plasmaspheric boundary layer. *Geophysical Research Letters*, *37*(7), L07106. https://doi.org/10.1029/2010GL042929

Mishin, E., & Sotnikov, V. (2017). The turbulent plasmasphere boundary layer and the outer radiation belt boundary. *Plasma Physics and Controlled Fusion*, *59*(12), 124003. https://doi.org/10.1088/1361-6587/aa8481

Mishin, E., & Streltsov, A. (2019). STEVE and the picket fence: Evidence of feedback-unstable magnetosphere-ionosphere interaction. *Geophysical Research Letters*, *46*(24), 14247–14255. https://doi.org/10.1029/2019GL085446

Mishin, E., & Streltsov, A. (2020). Prebreakup arc intensification due to short circuiting of mesoscale plasma flows over the plasmapause. *Journal of Geophysical Research: Space Physics*, *125*(5), e2019JA027666. https://doi.org/10.1029/2019JA027666

Mishin, E., & Streltsov, A. (2021a). Meso- and small-scale structure of the subauroral geospace. In C. Huang & G. Lu (Eds.), *Space physics and aeronomy collection V.3: Ionosphere dynamics and applications* (Vol. 260, pp. 135–154). Wiley & Sons. Geophysical Monograph Series. https://doi.org/10.1002/9781119507512.ch8

Mishin, E., & Streltsov, A. (2021b). *Nonlinear wave and plasma structures in the auroral and subauroral geospace*. Elsevier.

Mishin, E., & Streltsov, A. (2022). On the kinetic theory of subauroral arcs. *Journal of Geophysical Research: Space Physics*, *127*(8), e2022JA030667. https://doi.org/10.1029/2022JA030667

Mishin, E., & Streltsov, A. (2023). The inner structure of STEVE-linked SAID. *Geophysical Research Letters*, *50*(8), e2023GL102956. https://doi.org/10.1029/2023GL102956

Moffett, R., Ennis, A., Bailey, G., Heelis, R., & Brace, L. (1998). Electron temperatures during rapid subauroral ion drift events. *Annales Geophysicae*, *16*(4), 450–459. https://doi.org/10.1007/s00585-998-0450-x

Nishimura, Y., Dyer, A., Kangas, L., Donovan, E., & Angelopoulos, V. (2023). Unsolved problems in strong thermal emission velocity enhancement (STEVE) and the picket fence. *Frontiers in Astronomy and Space Science*, *10*, 1087974. https://doi.org/10.3389/fspas.2023.1087974

Nishimura, Y., Gallardo-Lacourt, B., Zou, Y., Mishin, E., Knudsen, D. J., Donovan, E. F., & Raybell, R. (2019). Magnetospheric signatures of STEVE: Implications for the magnetospheric energy source and interhemispheric conjugacy. *Geophysical Research Letters*, *46*(11), 5637–5644. https://doi.org/10.1029/2019GL082460

Nishimura, Y., Hussein, A., Erickson, P. J., Gallardo-Lacourt, B., & Angelopoulos, V. (2022). Statistical study of magnetospheric conditions for SAPS and SAID. *Geophysical Research Letters*, *49*(9), e2022GL098469. https://doi.org/10.1029/2022gl098469

Nishimura, Y., Lyons, L., Zou, S., Angelopoulos, V., & Mende, S. (2010). Substorm triggering by new plasma intrusion: THEMIS all-sky imager observations. *Journal of Geophysical Research*, *115*(A7), A07223. https://doi.org/10.1029/2009JA015166

Oksavik, K., Greenwald, R., Ruohoniemi, J., Hairston, M., Paxton, L., Baker, J., et al. (2006). First observations of the temporal/spatial variation of the sub-auroral polarization stream from the SuperDARN Wallops HF radar. *Geophysical Research Letters*, *33*(12), 12104. https://doi.org/10.1029/2006GL026256

Pavlov, A. (1996). Mechanisms of the electron density depletion in the SAR arc region. *Annales Geophysicae*, *14*(2), 211–221. https://doi.org/10.1007/s00585-996-0211-7

Pavlov, A., & Foster, J. (2001). Model/data comparison of F region ionospheric perturbation over Millstone Hill during the severe geomagnetic storm of July 15–16, 2000. *Journal of Geophysical Research*, *106*, 29051–29069. https://doi.org/10.1029/2000ja000387

Picone, J., Hedin, A., Drob, D., & Aikin, A. (2002). NRLMSISE-00 empirical model of the atmosphere: Statistical comparisons and scientific issues. *Journal of Geophysical Research*, *107*(A12), 1468. https://doi.org/10.1029/2002ja009430

Pokhotelov, O., Onishchenko, O., Sagdeev, R., & Treumann, R. (2003). Nonlinear dynamics of inertial Alfvén waves in the upper ionosphere: Parametric generation of electrostatic convective cells. *Journal of Geophysical Research*, *108*(A7), 1291. https://doi.org/10.1029/2003JA009888$09.00

Puhl-Quinn, P., Matsui, H., Mishin, E., Mouikis, C., Kistler, L., Khotyaintsev, Y., et al. (2007). Cluster and DMSP observations of SAID electric fields. *Journal of Geophysical Research*, *112*(A5), A05219. https://doi.org/10.1029/2006JA012065

Rees, M., & Roble, R. (1975). Observations and theory of the formation of stable auroral red arcs. *Reviews of Geophysics and Space Physics*, *13*(1), 201–242. https://doi.org/10.1029/rg013i001p00201

Schunk, R., Banks, P., & Raitt, W. (1976). Effect of electric fields and other processes upon the nighttime high-latitude F layer. *Journal of Geophysical Research*, *81*(19), 3271–3282. https://doi.org/10.1029/ja081i019p03271

Sinevich, A., Chernyshov, A., Chugunin, D., Clausen, L. B. N., Miloch, W. J., & Mogilevsky, M. M. (2023). Stratified subauroral ion drift (SSAID). *Journal of Geophysical Research: Space Physics*, *128*(3), e2022JA031109. https://doi.org/10.1029/2022JA031109

Spiro, R., Heelis, R., & Hanson, W. (1979). Rapid subauroral ion drifts observed by Atmospheric Explorer C. *Geophysical Research Letters*, *6*(8), 657–660. https://doi.org/10.1029/gl006i008p00657

Streltsov, A., & Mishin, E. (2018). Ultralow frequency electrodynamics of magnetosphere-ionosphere interactions near the plasmapause during substorms. *Journal of Geophysical Research: Space Physics*, *123*(9), 7441–7451. https://doi.org/10.1029/2018JA025899

Streltsov, A., & Mishin, E. (2022). Ionospheric feedback and ULF quarter-waves. *Journal of Geophysical Research: Space Physics*, *127*(9), e2022JA030659. https://doi.org/10.1029/2022JA030659

Titheridge, J. (2003). Ionization below the night F2 layer—A global model. *Journal of Atmospheric and Solar-Terrestial Physics*, *65*, 1035e1052. https://doi.org/10.1016/S1364-6826(03)00136-6

Trakhtengertz, V., & Feldstein, A. (1991). Turbulent Alfvén boundary layer in the polar ionosphere. 1. Excitation conditions and energetics. *Journal of Geophysical Research*, *96*(A11), 19363–19374. https://doi.org/10.1029/91ja00376

Wang, W., Yang, J., Nishimura, Y., Sun, W., Wei, D., Zhang, F., et al. (2021). Magnetospheric source and electric current system associated with intense SAIDs. *Geophysical Research Letters*, *48*(22), e2021GL093253. https://doi.org/10.1029/2021GL093253

Wang, Z., Zou, S., Shepherd, S. G., Liang, J., Gjerloev, J. W., Ruohoniemi, J. M., et al. (2019). Multi-instrument observations of mesoscale enhancement of subauroral polarization stream associated with an injection. *Journal of Geophysical Research: Space Physics*, *124*(3), 1770–1784. https://doi.org/10.1029/2019JA026535

Yadav, S., Shiokawa, K., Otsuka, Y., Connors, M., & St Maurice, J.-P. (2021). Multiwavelength imaging observations of STEVE at Athabasca, Canada. *Journal of Geophysical Research: Space Physics*, *126*(2), e2020JA028622. https://doi.org/10.1029/2020ja028622

Yizengaw, E., & Moldwin, M. (2005). The altitude extension of the mid-latitude trough and its correlation with plasmapause position. *Geophysical Research Letters*, *32*(9), L09105. https://doi.org/10.1029/2005GL022854